

Measuring Dipole Inversion in Self-Assembled Nano-Dielectric Molecular Layers

Li Zeng, Riccardo Turrisi, Bo Fu, Jonathan D. Emery, Amanda Walker, Mark A. Ratner, Mark C Hersam, Antonio Facchetti, Tobin J. Marks, and Michael J. Bedzyk

ACS Appl. Mater. Interfaces, **Just Accepted Manuscript** • DOI: 10.1021/acsami.7b16160 • Publication Date (Web): 29 Jan 2018

Downloaded from <http://pubs.acs.org> on February 5, 2018

Just Accepted

“Just Accepted” manuscripts have been peer-reviewed and accepted for publication. They are posted online prior to technical editing, formatting for publication and author proofing. The American Chemical Society provides “Just Accepted” as a service to the research community to expedite the dissemination of scientific material as soon as possible after acceptance. “Just Accepted” manuscripts appear in full in PDF format accompanied by an HTML abstract. “Just Accepted” manuscripts have been fully peer reviewed, but should not be considered the official version of record. They are citable by the Digital Object Identifier (DOI®). “Just Accepted” is an optional service offered to authors. Therefore, the “Just Accepted” Web site may not include all articles that will be published in the journal. After a manuscript is technically edited and formatted, it will be removed from the “Just Accepted” Web site and published as an ASAP article. Note that technical editing may introduce minor changes to the manuscript text and/or graphics which could affect content, and all legal disclaimers and ethical guidelines that apply to the journal pertain. ACS cannot be held responsible for errors or consequences arising from the use of information contained in these “Just Accepted” manuscripts.

Measuring Dipole Inversion in Self-Assembled Nano-Dielectric Molecular Layers

Li Zeng,^{1,2} Riccardo Turrisi,³ Bo Fu,⁴ Jonathan D. Emery,⁵ Amanda R. Walker,⁶ Mark A. Ratner,^{2,5,6} Mark C. Hersam,^{1,2,5,6} Antonio F. Facchetti,^{*,6} Tobin J. Marks,^{*,1,2,5,6} Michael J. Bedzyk^{*,1,2,4,5}

¹Applied Physics Program, Northwestern University, 2220 Campus Drive. Evanston, Illinois 60208, USA

²Materials Research Science and Engineering Center, Northwestern University, Evanston, Illinois 60208, USA

³Materials Science Department, University of Milano-Bicocca, Via R. Cozzi 53, 20126, Milan, Italy

⁴Department of Physics and Astronomy, Northwestern University, 2145 Sheridan Road, Evanston, Illinois 60208, USA

⁵Department of Materials Science and Engineering, Northwestern University, 2220 Campus Drive. Evanston, Illinois 60208, USA

⁶Department of Chemistry, Northwestern University, 2145 North Sheridan Road, Evanston, Illinois 60208, USA

Corresponding Authors:

E-mail: bedzyk@northwestern.edu (M.J.B.)

E-mail: t-marks@northwestern.edu (T.J.M.)

E-mail: a-facchetti@northwestern.edu (A.F.F.)

1
2
3
4 **ABSTRACT:** A self-assembled nano-dielectric (SAND) is an ultra-thin film, typically with
5 periodic layer-pairs of high- k oxide and phosphonic acid-based π -electron (PAE) molecular
6 layers. IPAE, having a molecular structure similar to PAE but with an inverted dipole direction,
7 has recently been developed for use in thin-film transistors. Here we report that replacing PAE
8 with IPAE in SAND-based thin-film transistors induces sizeable threshold and turn-on voltage
9 shifts, indicating the flipping of the built-in SAND polarity. The bromide counteranion (Br^-)
10 associated with the cationic stilbazolium portion of PAE or IPAE is of great importance because
11 its relative position strongly affects the electric dipole moment of the organic layer. Hence, a set
12 of X-ray synchrotron measurements were designed and performed to directly measure and
13 compare the Br^- distributions within the PAE and IPAE SANDs. Two trilayer SANDs, consisting
14 of a PAE or IPAE layer sandwiched between a HfO_x and a ZrO_x layer, were deposited on the
15 SiO_x surface of Si substrates or periodic Si/Mo multilayer substrates for X-ray reflectivity and X-
16 ray standing wave measurements, respectively. Along with complementary DFT simulations, the
17 spacings, elemental (Hf, Br, and Zr) distributions, molecular orientations, and Mulliken charge
18 distributions of the PAE and IPAE molecules within each of the SAND trilayers were determined
19 and correlated with the dipole inversion.
20
21
22
23
24
25
26
27
28
29
30
31
32
33
34
35
36
37
38
39
40
41
42
43
44
45
46

47 **KEYWORDS:** organic thin film transistor, dipole moment, dipole inversion, X-ray standing
48 waves, DFT, self-assembled monolayer
49
50
51
52
53
54
55
56
57
58
59
60

Introduction

Thin-film transistors (TFTs) based on both organic (OTFTs) and inorganic metal oxide (MOTFTs) semiconductors are considered to be excellent candidates for next-generation thin film electronics owing to their unique properties, such as low-cost, roll-to-roll fabrication by solution/printing methodologies, mechanical flexibility, optical transparency and compatibility with plastic substrates.¹⁻³ These attractive features make OTFT/MOTFTs ideal components for large-scale fabrication of several classes of unconventional devices such as flexible displays⁴⁻⁷, biocompatible circuits,⁸⁻¹⁰ and chemical sensors¹¹⁻¹³. However, despite these advantageous properties, there exist key limitations in this technology that remain to be solved, the foremost of which is the large operating voltages of most common solution-processable organic gate dielectrics used for OTFT fabrication and the high processing temperatures of those used for MOTFTs.^{2,14}

A typical TFT consists of a gate dielectric layer, a semiconductor layer, and three electrical contacts, i.e., source, drain, and gate (Fig. 1a). The basic TFT working principle is that the current between the source and drain contacts (I_{SD}) in the saturation region (Fig. 1b) is a function, for a given source-drain potential (V_{SD}), of the source-gate voltage V_G by the equation: $I_{SD} \propto \mu C (V_G - V_T)^2$, where V_T is the threshold voltage and μ , is the semiconductor carrier mobility.¹⁵ Typical TFT-based display technologies operate at < 20 V, and for portable/wearable electronic devices as well as radio-frequency systems, much lower operating voltages are required. Hence, for a given μ , larger TFT currents can be achieved at lower voltages if the gate dielectric capacitance (C) is sufficiently large. Since C is defined as $C = k\epsilon_0/d$ (where ϵ_0 is the vacuum permittivity, k is the dielectric constant and d is the film thickness), the capacitance can be

1
2
3 increased by using relatively high- k materials ($k > 10$) and/or by reducing dielectric thickness.
4
5 Various high capacitance materials are developed for both OTFTs and MOTFTs, such as high- k
6
7 polymers¹⁶⁻¹⁸, high- k metal oxide dielectrics¹⁹⁻²¹, and ultra-thin self-assembled monolayers²².
8
9
10 This Laboratory has developed a unique class of robust self-assembled nano-scale dielectrics
11
12 (SANDs) prepared by multi-layer coating/self-assembly. The previous generation of SANDs
13
14 were fabricated from a phosphonic acid-based π -electron molecular layer (PAE; $k \sim 9$)
15
16 sandwiched between two ultrathin high- k inorganic oxide layers.^{23,24,25} These organic-inorganic
17
18 hybrid dielectrics exhibit exceptionally large capacitance (400-1000 nF cm⁻²), good insulating
19
20 properties (10⁻⁵-10⁻⁷ A cm⁻² at 2 V), device consistency, and the possibility of ambient
21
22 atmospheric fabrication while only a few nms in thickness. A representative bottom gate
23
24 staggered TFT structure is shown in Fig. 1a. The device is constructed with Zr-SAND as the gate
25
26 dielectric, pentacene as the ~30-nm-thick channel layer material, a highly conductive Si substrate
27
28 as the gate electrode, and thermally evaporated Au contracts as the source and drain electrodes.
29
30
31 Fig. 1b presents the corresponding transistor performance curves demonstrating the compatibility
32
33 of SAND with low mobility organic semiconducting materials.²⁶ This device exhibits a field-
34
35 effect mobility of ~ 0.41 cm²/Vs, a current on-off ratio of $\sim 10^5$ and a threshold voltage of ~ -0.9
36
37 V as measure for the I-V characteristics and standard MOSFET equation.²⁷ Hence, the hybrid
38
39 nature of SANDs exploits the distinct properties of both the organic and inorganic components
40
41 and have been incorporated into low-operating voltage flexible semiconductor-based
42
43 OTFT/MOTFTs with enhanced performance.²³
44
45
46
47
48
49

50 Here we quantitatively investigate the electrical behavior of SANDs in context of the chemical
51
52 and structural aspects of their molecular/inorganic components.²³ The focus will be on
53
54 fundamental aspects of the dielectric behavior that remain unexplored, namely the built-in
55
56
57
58
59
60

1
2
3 polarity effects of the PAE molecule and details of important geometrical parameters. This
4 investigation will also serve to clarify findings from previous reports on how the dipolar
5 character of a self-assembled monolayer (SAM) affects the OTFT device performance.²⁸⁻³²
6
7 Typically, depositing a SAM on an oxide surface is known to decrease the leakage current and
8 reduce interfacial traps between the channel layer and dielectric layer.^{33,34} In particular, a well-
9 ordered SAM forms a dipolar layer that can alter and modify transistor parameters, particularly
10 the threshold voltage (V_T), and induce a gate potential shift by $\Delta V_T \sim NP_{\perp}/\epsilon_0 k$, where N is the
11 surface packing density, k is the dielectric constant of the SAM, and P_{\perp} is the molecular dipole
12 perpendicular to the substrate plane.^{29,35} Therefore, controlling the magnitude and direction of
13 P_{\perp} in a fabricated device is an important design criteria for next-generation electronics.³⁵⁻³⁷
14
15

16 To this end, we recently designed and synthesized a new molecule, IPAE, which is similar to
17 PAE in structure but possesses an “inverted” bond connectivity (Fig. 1c).³⁸ Note that the PAE
18 and IPAE molecules both consist of a positively charged π -conjugated stilbazolium unit
19 associated with a bromide (Br^-) counteranion for neutrality. Replacing PAE with IPAE during
20 the self-assembly step of dielectric fabrication yields an inverted SAND (I-SAND) multilayer
21 structure with an inverted dipole moment caused by flipping the regiochemistry of the molecular
22 building block. We recently found that the 4-layer ISAND exhibits a 40% higher k value for the
23 organic layer ($k_{\text{IPAE}} \sim 13$, whereas $k_{\text{PAE}} \sim 9$) and a 10% increased areal capacitance ($C_{\text{I-SAND}} \sim$
24 503 , whereas $C_{\text{SAND}} \sim 465 \text{ nF cm}^{-2}$) in comparison to the typical 4-layer Zr-SAND.^{24,38} OTFTs
25 fabricated based on inverted Zr-SAND (IZr-SAND) with p -type and n -type semiconductors also
26 exhibit sizable shifted threshold (V_T) and turn-on (V_{on}) voltages compared to those based on
27 conventional Zr-SAND.³⁸ These significant changes were rationalized by the built-in polarity
28 changes created by switching the organic component from PAE in the SAND to IPAE in I-
29
30
31
32
33
34
35
36
37
38
39
40
41
42
43
44
45
46
47
48
49
50
51
52
53
54
55
56
57
58
59
60

1
2
3 SAND. A deeper understanding on the origin of this “polarity switch” requires a
4
5 molecular/atomic-scale characterization that can structurally differentiate between the PAE- and
6
7 IPAE-based SANDs. In particular, the location of the halide counteranion associated with each
8
9 of these two building blocks is of great importance because it allows us to identify the negative
10
11 portion of each PAE/IPAE molecule, the molecular orientation and to understand the dipole
12
13 inversion and self-assembly deposition process. This information is essential to correlate changes
14
15 in charge transport with dipole-semiconductor interactions, which will ultimately lead to the
16
17 optimized design and engineering of future SAND-based devices.
18
19
20

21
22 To reduce the complexity that would arise from a typical 4-layer structure, we designed a direct
23
24 measurement to comprehensively analyze and compare the structure and halide counteranion
25
26 distribution in single layers of SAND and I-SAND. The characterization tools employed here are
27
28 a suite of X-ray techniques and complementary DFT simulations. We use X-ray reflectivity
29
30 (XRR) to probe the electron density profile of the trilayer, and extract the layer thicknesses,
31
32 densities, and interfacial sharpness.³⁹ Next, we determine the areal atomic densities of the Hf, Zr
33
34 and Br present in the film using X-ray fluorescence (XRF). Finally, we utilize the long-period X-
35
36 ray standing wave (XSW) technique – a measurement that is sensitive to the positions of the
37
38 XRF-measurable atomic species within the film – to precisely and accurately measure the
39
40 distribution profiles of the Hf, Zr and Br atoms within the film.⁴⁰⁻⁴⁴ DFT-optimized molecular
41
42 structures are also used to help visualize and interpret results derived from the X-ray
43
44 measurements.
45
46
47
48
49
50
51
52
53
54
55
56
57
58
59
60

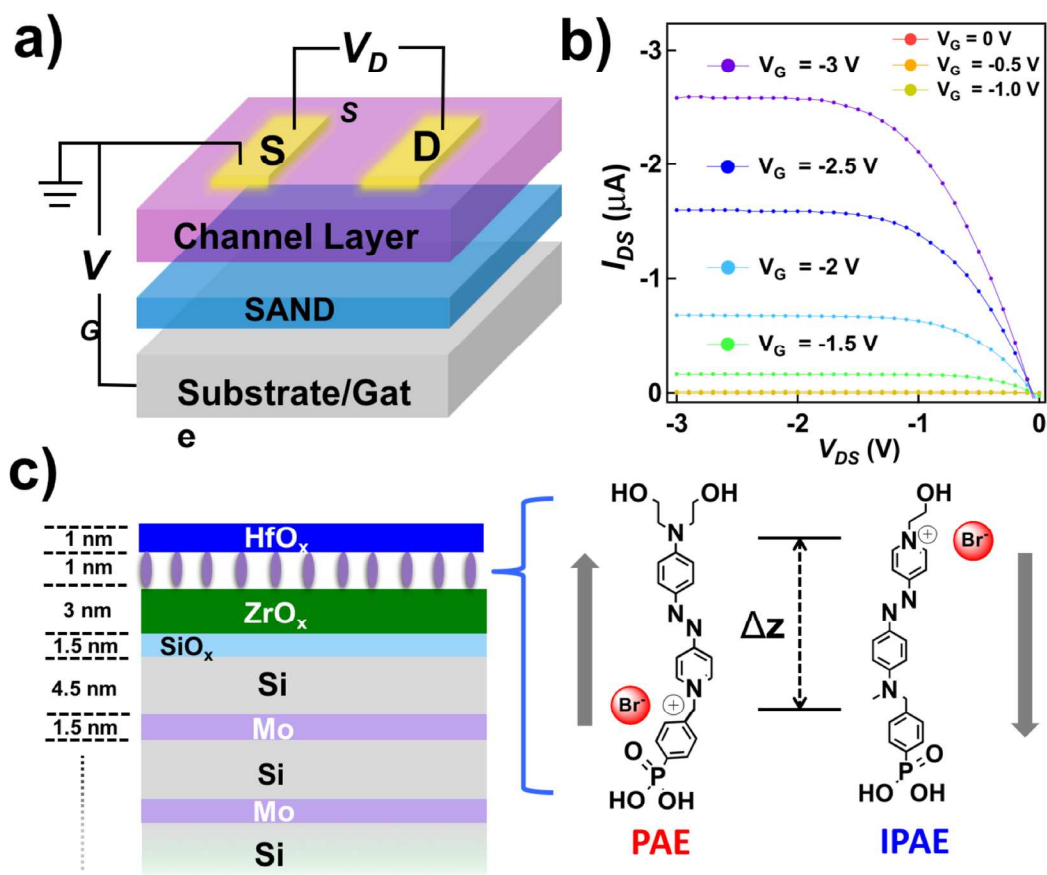


Figure 1. (a) Structure of a typical bottom gate staggered TFT with Zr-SAND as the gate dielectric. (b) A representative transistor curve of drain/source current I_{DS} as a function of drain/source voltage V_{DS} at multiple gate voltages V_G . (The TFT had pentacene as the semiconducting channel layer, and Zr-SAND as the dielectric.) (c) Side-view depiction of multilayer thin film structure with a HfO_x/ PAE or IPAE / ZrO_x SAND trilayer deposited on the SiO_x top-layer of a Si/Mo periodic multilayer. The grey arrow indicates the polarization direction. The Br⁻ counteranion layer height difference is indicated by Δz .

Experimental Section

Sample preparation

A trilayer SAND or I-SAND design containing a single PAE or IPAE layer sandwiched between a Zr oxide layer as the bottom prime layer and Hf oxide layer as the capping layer (as indicated in Fig. 1c) is utilized to facilitate structural analysis. The SAND or I-SAND trilayer films (Fig.

1
2
3 1c) were grown on Si substrates for XRR analysis and on Si/Mo multilayer substrates for XSW
4 analysis. Both substrates possessed a native SiO_x surface layer. The sputter deposited multilayer
5 substrate, which was designed to generate strong multilayer Bragg reflections, had 60 Si/Mo
6 bilayers (period $d = 6.0$ nm with Si: ~ 4.5 nm and Mo: ~ 1.5 nm) with Si as the topmost layer.⁴⁵⁻⁴⁷
7
8 Additional details about the synthesis of the trilayer SAND/I-SAND and Si/Mo multilayer
9 substrate are described in the Supporting Information (SI). Dielectric films were grown with the
10 same procedure on Si and Si/Mo so that the XRR-determined electron density profile could be
11 directly compared to the XSW-determined Hf, Br and Zr atomic distribution profiles for the
12 same film. XRF measurements of the Hf, Br and Zr coverages were made on Si/Mo substrate
13 samples.
14
15
16
17
18
19
20
21
22
23
24
25

26 **X-ray experimental details**

27
28 All X-ray measurements were performed at the Advanced Photon Source (APS) station 33BM-
29 C, where a Si(111) monochromator was used to select an 18.5 keV incident X-ray beam energy,
30 suitable for exciting Br K, Hf L and Zr K XRF, while avoiding the strong Mo K XRF from the
31 multilayer. In the XSW measurements, XRF spectra were collected at each incident angle with a
32 Vortex silicon drift detector (SSD) (Fig. S1a). A typical XRF spectrum collected during XSW
33 (at $\theta = 0.25^\circ$ and $Q = 0.82$ nm⁻¹) measurement from the SAND on Si/Mo is shown in Fig. S1b.
34
35 The reflected X-rays for the XRR and XSW measurements were collected with a Pilatus 100K
36 area detector. The intensity of reflected X-rays and background diffuse scatterings were recorded
37 by setting region of interests (ROIs) on the area detector. The samples were kept in an inert,
38 flowing He gas atmosphere throughout the experiment (Fig. S1a).
39
40
41
42
43
44
45
46
47
48
49
50
51

52 The X-ray reflectivity data from the SAND or I-SAND trilayers on Si substrates are presented in
53 Fig. S2. The derived electron density profiles³⁹ are used as the initial input for the XSW fitting
54
55
56
57
58
59
60

1
2
3 model of each trilayer type on the Si/Mo multilayer substrates. This trilayer/Si/Mo XRR analysis
4
5 used Parratt's recursion formulation⁴⁸ with an in-house developed least-squares fitting MATLAB
6
7 program.⁴¹ The absolute areal atomic density of three heavy elements are calculated from XRF
8
9 and listed in Table S1, indicating the overall similarity between SAND and I-SAND. The
10
11 electron densities and thicknesses of the HfO_x and ZrO_x layers from the XRR measurements of
12
13 SAND/ISAND on Si are consistent with the XRF determined Hf and Zr areal densities.
14
15

16
17 The Br⁻ counteranion layer mean heights $\langle z \rangle$ and height difference Δz for the SAND and I-SAND
18
19 trilayer films (Fig. 1c) were determined by X-ray standing wave (XSW) measurements.^{40,41,49,50}
20
21 The XSW was generated by the interference between the incident and reflected X-ray plane
22
23 waves from the periodic Si/Mo multilayer (Fig. 1c). The interference fringe visibility increases
24
25 dramatically when the reflectivity (R) approaches unity, which occurs at the total external
26
27 reflection (TER) condition and the first-order Bragg peak from this multilayer. The XSW
28
29 nodal/antinodal planes are parallel to the multilayer interfaces. Neglecting refraction effects from
30
31 the trilayer film, the XSW period is $D = 2\pi/Q$, where $Q = 4\pi \sin \theta / \lambda$ is the scattering vector,
32
33 λ is the X-ray wavelength, and θ is the incident angle. The TER condition and first-order
34
35 multilayer Bragg peak occur at relatively low values of Q, producing a variable period for the
36
37 XSW between 5 and 30 nm for this $d = 6 \text{ nm}$ multilayer. In addition to the XSW period
38
39 decreasing as Q (or θ) is advanced, the XSW phase, v , also decreases by π radians as the
40
41 incident angle θ is scanned across the TER and Bragg reflection regions. This causes an inward
42
43 shift (along the z-axis) of the XSW E-field intensity, which can be approximated with the 2-
44
45 beam interference function⁵¹ as:
46
47
48
49
50
51

$$I(Q, z) = 1 + R + 2\sqrt{R} \cos(v - Qz). \quad (1)$$

52
53
54
55
56
57
58
59
60

1
2
3 While the X-ray fluorescence (XRF) yield, from each XRF-selected elemental distribution
4 profile, $\rho(z)$, is,
5
6

$$Y(Q) = \int I(Q, z) \rho(z) dz. \quad (2)$$

7
8
9
10
11 Eqs. 1 and 2 can be calculated by a modification⁴¹ to Parratt's recursion formulation.⁴⁸ A more
12 rigorous derivation, which we use for analyzing the data, takes into account refraction and
13 absorption affects within the trilayer film, and is described elsewhere.⁴¹ Quantitative structural
14 information is derived by best-fits of $\rho(z)$ model-based yields using Eq. 2 to the measured XSW
15 yields for Zr, Br and Hf. By comparing the atomic distribution profiles extracted from XSW, we
16 seek to locate Br⁻ counteranion positions relative to Zr and Hf in both SAND and I-SAND and
17 quantify dipolar inversion when switching from PAE to IPAE molecules.
18
19
20
21
22
23
24
25
26

27 **DFT Simulations**

28
29
30 Density functional theory (DFT) was employed to find the most probable configurations of PAE
31 and IPAE by minimizing the total energy E of each isolated molecule.^{52,53} Since the Br⁻ position
32 is subjected to the molecular orientation and tilting, a Boltzmann probability distribution
33
34
35
36
37 $P_B = e^{\left[\frac{E - E_{min}}{k_B T} \right]}$ is defined to evaluate the chances of other molecular configurations, where E_{min}
38 is the total energy of the optimized structure, k_B is the Boltzmann constant and T is set at 300 K.
39
40
41
42 The degree of molecular tilting is characterized by z_{N^+} , which is defined as the distance between
43 the +1 quaternized nitrogen in the pyridine group and the bottom plane formed by the three
44 oxygen atoms of PAE or IPAE molecule discussed below. The Boltzmann probability $P_B =$
45
46
47
48
49 $e^{\left[\frac{E(z_{N^+}) - E_{min}}{k_B T} \right]}$ corresponding to different z_{N^+} values is calculated from the total energy $E(z_{N^+})$
50
51
52
53
54
55
56
57
58
59
60

supplementary information (SI). Since Br^- is expected to be located near the quaternized nitrogen (Fig. 1c), the probability distributions should be highly correlated to the Br^- distributions in PAE and IPAE.

Results and Discussion

The XRR data for both SAND (red circles) and I-SAND (blue circles) on Si/Mo multilayers are presented in Fig. 2. The reflectivity is plotted as a function of scattering vector magnitude Q and compared to a model fit. Intensities for the first three Bragg peaks (1st to 3rd orders) at $Q = 1.17$, 2.24 and 3.33 nm^{-1} are measured to accurately calculate the multilayer period. The 1st order

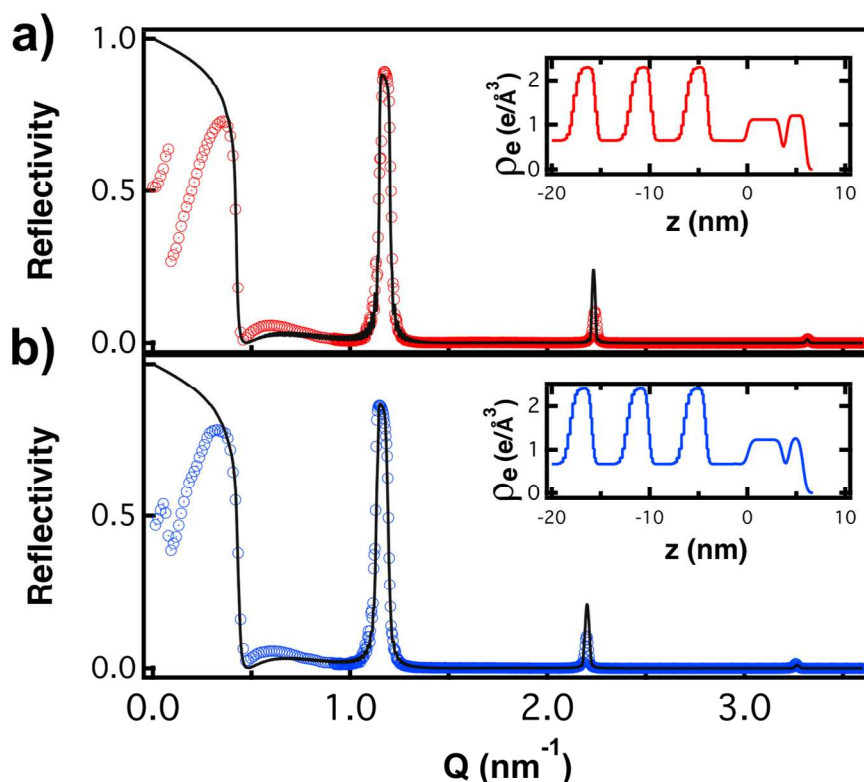
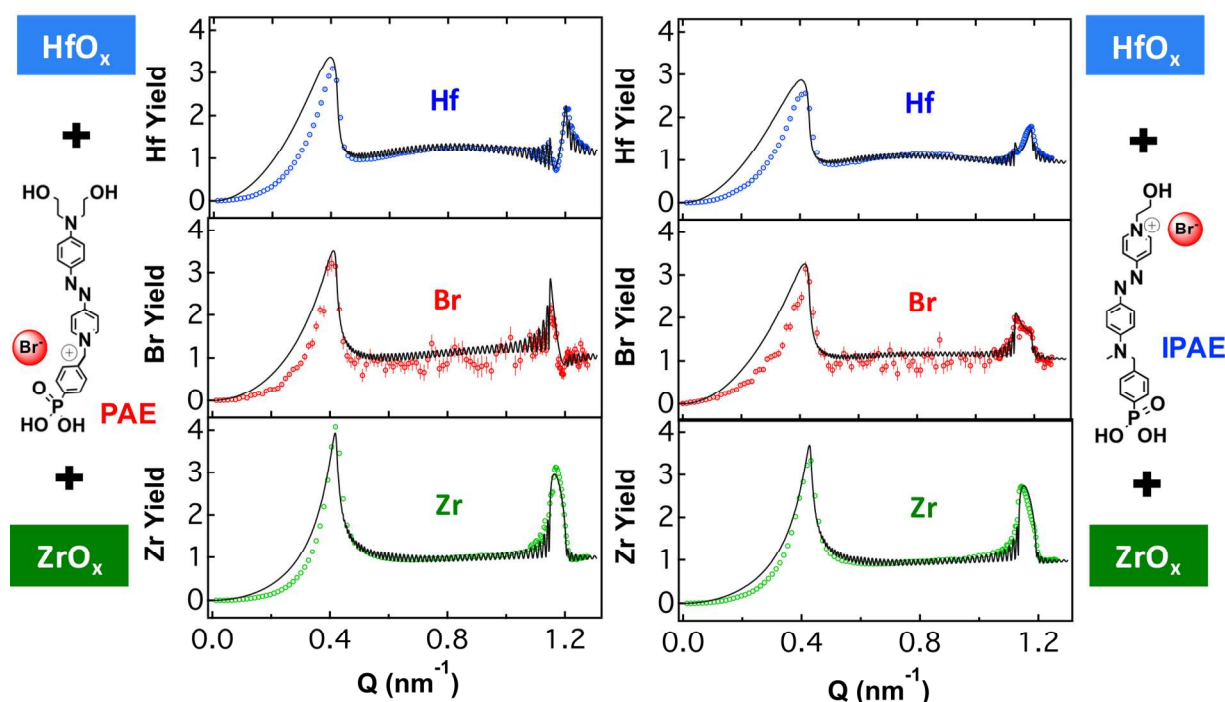


Figure 2. X-ray reflectivity data (open circles) and fits (solid black lines) for the (a) $\text{HfO}_x/\text{PAE}/\text{ZrO}_x$ and (b) $\text{HfO}_x/\text{IPAE}/\text{ZrO}_x$ trilayers deposited on the SiO_x top-layer of Si/Mo periodic multilayer. The insets show the respective top several layers of electron density profile determined from the XRR fits with the z -axis origin chosen to be located at the $\text{SiO}_x/\text{ZrO}_x$ interface.

Bragg peak has a high reflected intensity of $R_{max} = 85\%$, indicating well-ordered periodic multilayers with sharp interfaces. The black solid lines are the best-fit results of data between $Q = 0.4$ and 3.5 nm^{-1} . In the low- Q region ($Q < 0.4 \text{ nm}^{-1}$), the X-ray beam footprint over-extends the length of sample, which leads to the deviation of experimental data from the theory. The insets in Fig. 2 show XRR-determined electron density ρ_e profiles for SAND and I-SAND trilayers on Si/Mo multilayers. The profile region from $z = 0$ to 6 nm corresponds to the trilayer SAND or I-SAND, which are derived from XRR measurements of their counterparts on the Si substrates. The alternating low and high e -density regions below $z = 0$ match closely to the expected bulk values for SiO_2 , Si and Mo of 0.70 , 0.71 and $2.56 \text{ e}/\text{\AA}^3$, respectively.

The XSW analysis is conducted in the Q -region for total external reflection (TER) (0^{th} order Bragg peak) and the 1^{st} order Bragg peak. The 2^{nd} and 3^{rd} order reflections are omitted because of their low reflectivity. These normalized fluorescence yields for the Hf $L\alpha$, Br $K\alpha$, and Zr $K\alpha$ from both the SAND and I-SAND samples are plotted in Fig. 3. Qualitatively, each elemental



1
2
3 **Figure 3.** XSW induced normalized XRF yields of Hf (blue), Br (red) and Zr (green) (from the
4 top to bottom) for both $\text{HfO}_x / \text{PAE} / \text{ZrO}_x$ (left) and $\text{HfO}_x / \text{IPAE} / \text{ZrO}_x$ (right) trilayer
5 SAND/ISAND on Si/Mo multilayer substrates. These data were collected simultaneously with the
6 reflectivity data shown in Fig. 2. The solid lines are fits to the data based on the model described
7 in Fig. 4a.
8
9

10
11
12 normalized yield exhibits a strong, characteristic XSW-induced modulation across the 1st order
13 Bragg peak indicating distinctively different distributions for each atomic species. Note that,
14 from Eqs. 1 and 2, a completely random distribution would exhibit a modulation that simply
15 follows $1 + R(Q)$, where the reflectivity $R(Q)$ can be seen in Fig. 2. The distinctive asymmetric
16 shapes observable in Fig. 3 indicate that each of the atomic distribution profiles, as projected
17 onto the z -axis from an ensemble-averaged 8-mm² X-ray footprint, is confined to a well-defined
18 nm-scale distribution within the dielectric film. While the Zr XSW modulations at the Bragg
19 peak for both SAND and I-SAND are qualitatively similar, the Hf and Br modulations differ
20 substantially between the conventional and inverted structures. Note that the normalized Br
21 fluorescence yields for I-SAND film present an interesting atypical feature while the other
22 fluorescence yields show a typical XSW oscillation across the Bragg peak. This is related to the
23 broader Br elemental distribution profile (Fig. 4a) when modeled with a Gaussian function and
24 the DFT-optimized molecular structure that will be discussed below.
25
26
27
28
29
30
31
32
33
34
35
36
37
38
39
40
41
42

43 Quantitative analysis of the XSW data allows us to determine the atomic distributions
44 $\rho_{\text{Hf}}(z)$, $\rho_{\text{Br}}(z)$, and $\rho_{\text{Zr}}(z)$ and to create an elementally sensitive thin film profile. Due the
45 footprint effect discussed above, the XSW analysis focuses on the $Q > 0.4 \text{ nm}^{-1}$ data range. We
46 model both ρ_{Hf} and ρ_{Br} as Gaussian distributions with two fitting parameters: mean positions z_M
47 and widths σ_M . For the thicker ZrO_x layer, ρ_{Zr} is modeled with a rectangular function convoluted
48 with a Gaussian, with free parameters for the thickness t_{Zr} and the interfacial width σ_{Zr} . Each
49
50
51
52
53
54
55
56
57
58
59
60

distribution also includes an extended uniform distribution $\rho_{EM}(z)$ to account for the atoms that are not contained within the modeled distributions. This could result from minor inhomogeneities across the solution-processed film (X-ray probing area $\sim 8 \text{ mm}^2$), and fluorescence signals generated by incoherent diffuse scattered X-rays.^{46,47} The range is set from $z = 0$ to 10 nm to account for a minority-disordered fraction of atoms that are randomly distributed within the film. The final model distribution is therefore $\rho(z) = C \rho_M(z) + (1 - C) \rho_{EM}(z)$, where C is the ordered fraction and $\rho_M(z)$ is the distribution profile for $M = \text{Hf, Br, or Zr}$. From the above model for each element and the calculated E -field intensities, $I(Q, z)$, the best-fit results of normalized fluorescence yields are generated and plotted in Fig. 3 with solid black lines. The TER region has a continually decreasing XSW period from infinity to $2\pi/Q_c \sim 14 \text{ nm}$, which helps constrain the dimensions of the thick ZrO_x primer layer.⁴⁰ As for the other two elemental distributions, the first Bragg peak is the primary sensitive fitting range. The XSW

Table 1. Model parameters obtained from the fits for the XSW results in Fig. 3. The ZrO_x layer is modeled with a layer thickness t_{Zr} and interfacial width σ_{Zr} . The Hf (Br) elemental distribution is modeled by a Gaussian profile with mean position z_{Hf} (z_{Br}) and width σ_{Hf} (σ_{Br}). An ordered fraction C is also defined in the distribution model for all three elements.

	t_{Zr} (nm)	σ_{Zr} (nm)	C_{Zr}	z_{Br} (nm)	σ_{Br} (nm)	C_{Br}	z_{Hf} (nm)	σ_{Hf} (nm)	C_{Hf}
PAE	3.2	0.4	0.9	4.3	0.6	0.9	5.3	0.6	1.0
IPAE	3.6	0.6	1.0	4.6	1.5	0.8	5.3	1.2	0.9

model fit determined atomic distributions with $z = 0$ at the $\text{SiO}_x/\text{ZrO}_x$ interface are shown in Fig. 4a. The three elements show up in the expected sequence within each trilayer. The vertical green dash line denotes the top surface of ZrO_x layer, and the red and blue dash lines denote the peak

1
2
3 positions for the Br and Hf atomic distributions for both the SAND and I-SAND cases. The Hf
4 and Zr results yield reasonable fits in Fig. 3 indicating the accuracy of this XSW measurement.
5
6
7 The best-fit results are summarized in Table 1. As indicated by the arrows in Fig. 4a, when
8 replacing PAE with IPAE in the trilayer SANDs, the Br peak position shifts outward by 0.2 nm
9 from the top ZrO_x surface and the Br peak moves 0.5 nm closer to the HfO_x peak. A slightly
10 wider elemental distribution of I-SAND compared to SAND is observed. This may partially be
11 due to the elemental distributions being averaged across the mm^2 area illuminated by the incident
12 X-ray beam. However, the peak position remains valid since it shows the most probable location.
13
14
15
16
17
18
19
20
21
22
23
24
25
26
27
28
29
30
31
32
33
34
35
36
37
38
39
40
41
42
43
44
45
46
47
48
49
50
51
52
53
54
55
56
57
58
59
60

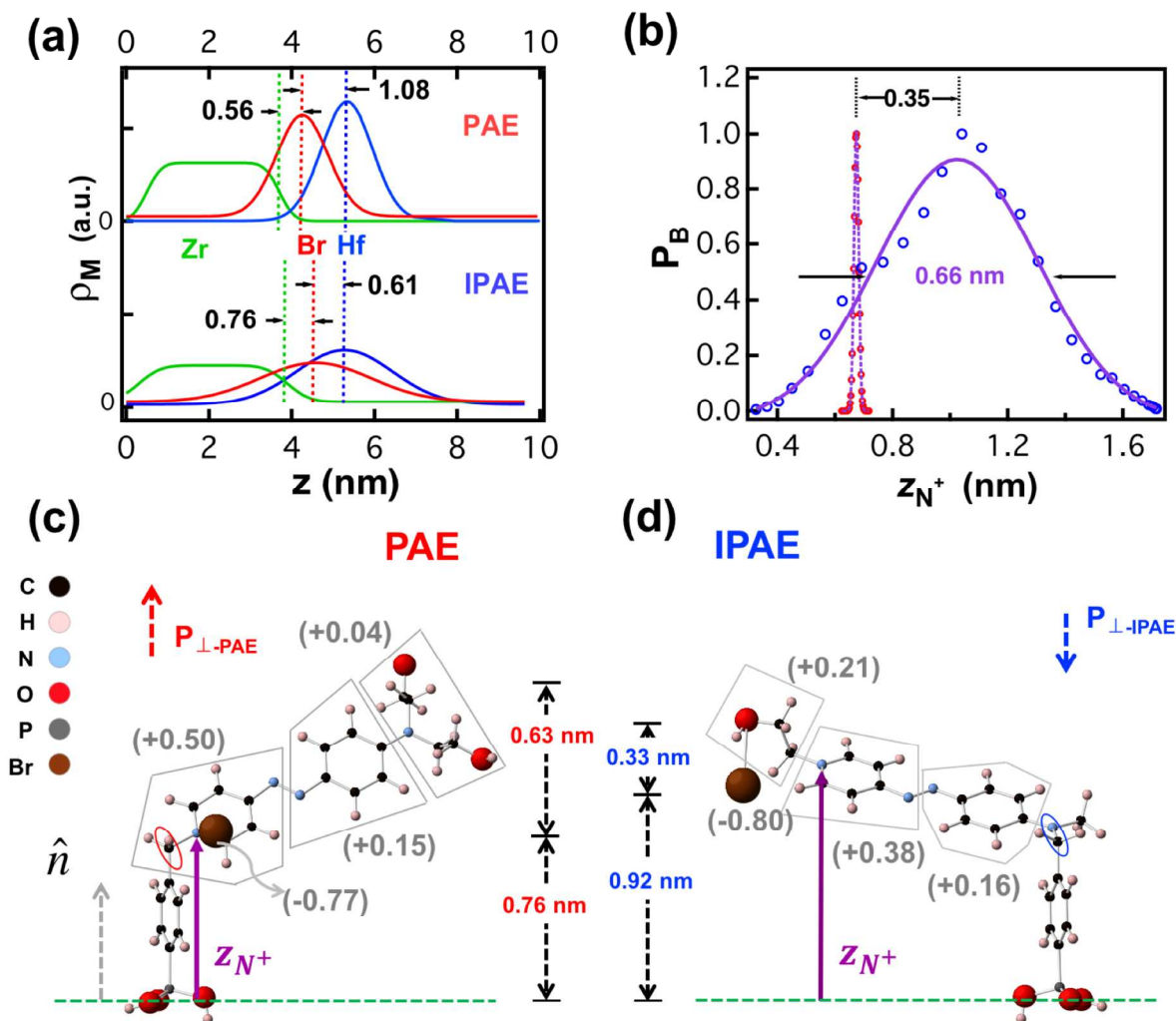


Figure 4. (a) XSW-determined elemental distribution profiles from Eq. 2 and Fig. 3 for Zr (green line), Br (red line) and Hf (blue line) for both $\text{HfO}_x/\text{PAE}/\text{ZrO}_x$ (upper) and $\text{HfO}_x/\text{IPAE}/\text{ZrO}_x$ (down) trilayer SAND on Si/Mo multilayer substrates. (b) The DFT-calculated Boltzmann probability distribution P_B for PAE (red circles) and IPAE (blue circles) along with Gaussian-fits. The DFT-optimized molecular structures of PAE (c) and IPAE (d). The height z_{N^+} of quaternized nitrogen (N^+) is defined by the purple arrow. Green dash lines represent the planes formed by the three oxygens at each phosphonic acid end. Net charges from Mulliken analysis are labeled for each moiety selected with grey solid lines. The bottom unselected parts of PAE and IPAE have net charges close to 0.

Complementary DFT simulations explored the molecular configurations of individual anchored

1
2
3 PAE and IPAE moieties, and provide additional insight into the measured elemental distribution
4 profiles. The optimized structures are shown in Figs 4c and d. Assuming the ZrO_x top surface is
5 terminated with the plane formed by three oxygens of the phosphonic ends (green dash lines in
6 Figs. 4c and 4d)), the long molecular axes of both individual molecules are significantly tilted
7 with respect to the surface normal direction (\hat{n}). These simulations predict the thickness of the
8 molecular layer are ~ 1.39 nm for PAE and ~ 1.25 nm for IPAE. Note that the DFT-calculated
9 molecular heights, which do not include the neighboring molecular interactions, agree with the
10 XRR-determined thickness of the organic layer thickness: 1.15 nm for PAE and 1.0 nm for
11 IPAE. The smaller height of IPAE vs PAE is also in consistent with XSW measurement which
12 finds a 1.6 nm distance between the ZrO_x surface and the peak position of the ρ_{Hf} profile for the
13 PAE compared to 1.4 nm for the IPAE. DFT also predicts the optimum position of Br^- in IPAE is
14 higher than that in PAE (0.92 nm vs. 0.76 nm), and closer to the bottom of the capping HfO_x
15 layer (0.33 vs 0.66 nm). This is in accord with the XSW-derived Br peak positions, and the
16 relative distances to the oxide layers shown in Fig. 4a. The XSW-derived Br elemental
17 distribution in the IPAE molecule presents a larger distribution width (1.5 nm) than that in PAE
18 (0.6 nm). Possible causes for this result are elucidated by the DFT-computed probability
19 distribution P_B and Mulliken charge analysis. The Br^- is considered to be vertically co-located
20 with the quaternized nitrogen (N^+) atom of the pyridinium ring for PAE or IPAE shown in Figs.
21 4c and 4d. Therefore, the distribution of Br^- is strongly influenced by the magnitude of the tilting
22 of the long molecular. This effect is expected to be more profound in the IPAE molecule because
23 its pyridine group and Br^- are positioned near the free end of the molecule. For the IPAE
24 molecule, the part highlighted by a blue circle in Fig. 4d, consists of one nitrogen atom and one
25 carbon atom. The sp^3 -hybridized bonds of these two adjacent atoms allow freedom of rotation
26
27
28
29
30
31
32
33
34
35
36
37
38
39
40
41
42
43
44
45
46
47
48
49
50
51
52
53
54
55
56
57
58
59
60

(Fig. S5a), which leads to the variation of the N^+ height z_{N^+} and subsequently the Br^- position. P_B , shown in Fig. 4b indicates the motion of N^+ has ~ 0.66 nm vertical height distribution. Similarly, the z_{N^+} distribution for the PAE molecule yields a much narrower width (~ 0.02 nm). This is due to the relatively rigid sp^3 bond angle of the carbon atom, highlighted inside the red circle (Fig. 4c). Hence, an additional ~ 0.64 nm difference leads Br^- to have a broader distribution in IPAE than in PAE.

Another reason for the broader distribution of Br^- within I-SAND may be explained by the Mulliken charge analysis presented in Figs. 4c and d, which probes the majority positive charges of the cations of both molecules. As indicated by the net charge distribution, the cation in PAE has a more localized positive charge compared to that in IPAE. Therefore, the Br^- counteranion associated with PAE distributes more locally around the N^+ due to the stronger electrostatic attractive force, and a narrower Br^- distribution is expected. This result suggests that the DFT simulation results are in a reasonable agreement with the XSW experimental findings regarding the molecular configuration and Br^- anion distributions. The dipole moments of PAE and IPAE were also computed from the Mulliken charge analysis and are compiled in Table S4. The projected magnitude along the surface normal direction P_{\perp} are 3.04 and -0.70 D for the optimized PAE and IPAE structures, respectively. The negative sign indicates the inversion of dipole direction as shown by the arrows in Figs. 4c and 4d. Note that the experimental results show that when replacing PAE with IPAE molecular layer in SAND-based device, an additional negative shift in threshold voltage ΔV_T was observed.³⁸ This is consistent with the relationship, $\Delta V_T \sim NP_{\perp}/\epsilon_0 k$. These results show that, through design and control of the dipole inversion, characterized by XSW measurements and DFT simulations, and demonstrated with OTFTs device performances, provide more flexibility in operating more complex devices.

Conclusions

A direct comparison of counteranion distributions within two self-assembled nano-dielectrics (SANDs) has been characterized and systematically studied by X-ray technique (XRR, XRF, and XSW) and complementary DFT simulation. The two SANDs share the same trilayer structures: a self-assembled high- k molecular layer of inverting dipole, and each sandwiched between a capping HfO_x layer and a bottom ZrO_x layer. The organic layer spacing from X-ray measurement is in a good agreement with DFT-optimized molecular height, indicating both molecules are tilted with respect the surface normal direction. The Br^- counteranions of PAE molecules are found to locate closer to the bottom ZrO_x layer and have a narrower distribution compared to that in IPAE. This result is in reasonable agreement with DFT simulations of the degree of molecular tilting, and with the results of Mulliken charge analysis. The experimental and computational results reveal how PAE and IPAE self-assemble and orient within SAND and I-SAND, and correlated the dipole inversion to the controlled voltage shifts when using IPAE as a polarizable layer in devices.

Supporting information

Supporting Information is available free of charge on the [ACS Publications website](#) at DOI: [XXXXXXXXXXXXX](#).

Detailed synthetic methods for the Si/Mo multilayer substrate and trilayer films, experimental setup for the X-ray standing wave measurements and a representative X-ray fluorescence (XRF) spectrum, X-ray reflectivity (XRR) results for two trilayer films deposited on Si substrates, comparison of atomic and electron areal densities derived from both XRR and XRF measurements, and details of the density functional theory (DFT) simulations, the optimized structures of PAE and IPAE molecules, Mulliken charge analysis, and computed dipole moments.

AUTHOR INFORMATION

Corresponding Authors

E-mail: bedzyk@northwestern.edu (M.J.B.)

E-mail: t-marks@northwestern.edu (T.J.M.)

1
2
3 E-mail: a-facchetti@northwestern.edu (A.F.F.)
4

5 **ORCID**

6 Tobin J. Marks: 0000-0001-8771-0141

7
8 Michael J. Bedzyk: 0000-0002-1026-4558

9
10 Li Zeng: 0000-0001-6390-0370
11
12
13

14 **Notes**

15 The authors declare no competing financial interest.
16

17 **Acknowledgements**

18
19 This research was supported by the Northwestern University MRSEC (NSF DMR-1121262).
20 XSW and XRR measurements were performed at 33BM-C of the Advanced Photon Source
21 (APS) of Argonne National Lab, supported by DOE under grant number DE-AC02-06CH11357.
22
23 A.F. thanks the Shenzhen Peacock Plan project (KQTD20140 630110339343) and AFOSR
24 (FA95501510044) for financial support. We also gratefully acknowledge the computational
25 resources from the Quest high performance computing facility at Northwestern University and
26 the Extreme Science and Engineering Discovery Environment (XSEDE) program, which is
27 supported by National Science Foundation grant number ACI-1053575. We thank Dr. Chian Liu
28 and Dr. Bing Shi from the APS Optics Group for the deposition of Si/Mo multilayer substrates.
29
30
31
32
33
34
35
36

37 **References**

- 38
39 (1) Ortiz, R. P.; Facchetti, A. F.; Marks, T. J. High-K Organic, Inorganic, and Hybrid Dielectrics
40 for Low-Voltage Organic Field-Effect Transistors. *Chem. Rev.* **2010**, *110*, 205-239.
41 (2) Yu, X.; Marks, T. J.; Facchetti, A. Metal Oxides for Optoelectronic Applications. *Nat. Mater.*
42 **2016**, *15*, 383-396.
43 (3) Nomura, K.; Ohta, H.; Takagi, A.; Kamiya, T.; Hirano, M.; Hosono, H. Room-Temperature
44 Fabrication of Transparent Flexible Thin-Film Transistors Using Amorphous Oxide
45 Semiconductors. *Nature* **2004**, *432*, 488-492.
46 (4) Printz, A. D.; Lipomi, D. J. Competition between Deformability and Charge Transport in
47 Semiconducting Polymers for Flexible and Stretchable Electronics. *Applied Physics Reviews*
48 **2016**, *3*, 021302.
49 (5) Sharma, B. K.; Ahn, J.-H. Flexible and Stretchable Oxide Electronics. *Adv. Electron. Mater.*
50 **2016**, *2*, 1600105.
51 (6) Wang, G.; Persson, N.; Chu, P.-H.; Kleinhenz, N.; Fu, B.; Chang, M.; Deb, N.; Mao, Y.;
52 Wang, H.; Grover, M. A. Microfluidic Crystal Engineering of Π -Conjugated Polymers. *ACS*
53 *Nano* **2015**, *9*, 8220-8230.
54
55
56
57
58
59
60

- (7) Jun, S.; Ju, B.-K.; Kim, J.-W. Fabrication of Substrate-Free Double-Side Emitting Flexible Device Based on Silver Nanowire-Polymer Composite Electrode. *Current Applied Physics* **2017**, *17*, 6-10.
- (8) Rogers, J. A.; Someya, T.; Huang, Y. Materials and Mechanics for Stretchable Electronics. *Science* **2010**, *327*, 1603-1607.
- (9) Hammock, M. L.; Chortos, A.; Tee, B. C.; Tok, J. B.; Bao, Z. 25th Anniversary Article: The Evolution of Electronic Skin (E-Skin): A Brief History, Design Considerations, and Recent Progress. *Adv. Mater.* **2013**, *25*, 5997-6038.
- (10) Lei, T.; Guan, M.; Liu, J.; Lin, H.-C.; Pfattner, R.; Shaw, L.; McGuire, A. F.; Huang, T.-C.; Shao, L.; Cheng, K.-T. Biocompatible and Totally Disintegrable Semiconducting Polymer for Ultrathin and Ultralightweight Transient Electronics. *Proceedings of the National Academy of Sciences* **2017**, *114*, 5107-5112.
- (11) Zhang, J.; Liu, X.; Neri, G.; Pinna, N. Nanostructured Materials for Room-Temperature Gas Sensors. *Adv. Mater.* **2016**, *28*, 795-831.
- (12) Wang, B.; Ding, J.; Zhu, T.; Huang, W.; Cui, Z.; Chen, J.; Huang, L.; Chi, L. Fast Patterning of Oriented Organic Microstripes for Field-Effect Ammonia Gas Sensors. *Nanoscale* **2016**, *8*, 3954-3961.
- (13) Huang, W.; Zhuang, X.; Melkonyan, F. S.; Wang, B.; Zeng, L.; Wang, G.; Han, S.; Bedzyk, M. J.; Yu, J.; Marks, T. J. Uv-Ozone Interfacial Modification in Organic Transistors for High - Sensitivity NO₂ Detection. *Adv. Mater.* **2017**, *29*, 1701706.
- (14) Kamiya, T.; Nomura, K.; Hosono, H. Present Status of Amorphous In-Ga-Zn-O Thin-Film Transistors. *Science and Technology of Advanced Materials* **2010**, *11*, 044305.
- (15) DiBenedetto, S. A.; Facchetti, A.; Ratner, M. A.; Marks, T. J. Molecular Self - Assembled Monolayers and Multilayers for Organic and Unconventional Inorganic Thin - Film Transistor Applications. *Adv. Mater.* **2009**, *21*, 1407-1433.
- (16) Bucella, S. G.; Luzio, A.; Gann, E.; Thomsen, L.; McNeill, C. R.; Pace, G.; Perinot, A.; Chen, Z.; Facchetti, A.; Caironi, M. Macroscopic and High-Throughput Printing of Aligned Nanostructured Polymer Semiconductors for Mhz Large-Area Electronics. *Nat. Commun.* **2015**, *6*, 8394.
- (17) Chu, P. H.; Wang, G.; Fu, B.; Choi, D.; Park, J. O.; Srinivasarao, M.; Reichmanis, E. Synergistic Effect of Regioregular and Regiorandom Poly (3 - Hexylthiophene) Blends for High Performance Flexible Organic Field Effect Transistors. *Adv. Electron. Mater.* **2016**, *2*, 1500384.
- (18) Adhikari, J. M.; Gadinski, M. R.; Li, Q.; Sun, K. G.; Reyes - Martinez, M. A.; Iagodkine, E.; Briseno, A. L.; Jackson, T. N.; Wang, Q.; Gomez, E. D. Controlling Chain Conformations of High - K Fluoropolymer Dielectrics to Enhance Charge Mobilities in Rubrene Single - Crystal Field - Effect Transistors. *Adv. Mater.* **2016**, *28*, 10095-10102.
- (19) Arnold, H. N.; Cress, C. D.; McMorrow, J. J.; Schmucker, S. W.; Sangwan, V. K.; Jaber-Ansari, L.; Kumar, R.; Puntambekar, K. P.; Luck, K. A.; Marks, T. J. Tunable Radiation Response in Hybrid Organic-Inorganic Gate Dielectrics for Low-Voltage Graphene Electronics. *ACS Appl. Mater. Interfaces* **2016**, *8*, 5058-5064.
- (20) Robertson, J. High Dielectric Constant Oxides. *The European Physical Journal Applied Physics* **2004**, *28*, 265-291.
- (21) Balendhran, S.; Deng, J.; Ou, J. Z.; Walia, S.; Scott, J.; Tang, J.; Wang, K. L.; Field, M. R.; Russo, S.; Zhuiykov, S. Enhanced Charge Carrier Mobility in Two - Dimensional High Dielectric Molybdenum Oxide. *Adv. Mater.* **2013**, *25*, 109-114.

- 1
2
3 (22) Casalini, S.; Bortolotti, C. A.; Leonardi, F.; Biscarini, F. Self-Assembled Monolayers in
4 Organic Electronics. *Chem. Soc. Rev.* **2017**, *46*, 40-71.
- 5 (23) Ha, Y. G.; Everaerts, K.; Hersam, M. C.; Marks, T. J. Hybrid Gate Dielectric Materials for
6 Unconventional Electronic Circuitry. *Acc. Chem. Res.* **2014**, *47*, 1019-1028.
- 7 (24) Chakhalian, J.; Rondinelli, J. M.; Liu, J.; Gray, B. A.; Kareev, M.; Moon, E. J.; Prasai, N.;
8 Cohn, J. L.; Varela, M.; Tung, I. C.; Bedzyk, M. J.; Altendorf, S. G.; Strigari, F.; Dabrowski, B.;
9 Tjeng, L. H.; Ryan, P. J.; Freeland, J. W. Asymmetric Orbital-Lattice Interactions in Ultrathin
10 Correlated Oxide Films. *Phys. Rev. Lett.* **2011**, *107*.
- 11 (25) Everaerts, K.; Emery, J. D.; Jariwala, D.; Karmel, H. J.; Sangwan, V. K.; Prabhumirashi, P.
12 L.; Geier, M. L.; McMorrow, J. J.; Bedzyk, M. J.; Facchetti, A.; Hersam, M. C.; Marks, T. J.
13 Ambient-Processable High Capacitance Hafnia-Organic Self-Assembled Nanodielectrics. *J. Am.*
14 *Chem. Soc.* **2013**, *135*, 8926-8939.
- 15 (26) Ha, Y. G.; Emery, J. D.; Bedzyk, M. J.; Usta, H.; Facchetti, A.; Marks, T. J. Solution-
16 Deposited Organic-Inorganic Hybrid Multilayer Gate Dielectrics. Design, Synthesis,
17 Microstructures, and Electrical Properties with Thin-Film Transistors. *J. Am. Chem. Soc.* **2011**,
18 *133*, 10239-10250.
- 19 (27) Sze, S. M.: *Semiconductor Devices: Physics and Technology*; John Wiley & Sons, 2008.
- 20 (28) Martinez Hardigree, J. F.; Katz, H. E. Through Thick and Thin: Tuning the Threshold
21 Voltage in Organic Field-Effect Transistors. *Acc. Chem. Res.* **2014**, *47*, 1369-1377.
- 22 (29) Possanner, S. K.; Zojer, K.; Pacher, P.; Zojer, E.; Schürer, F. Threshold Voltage Shifts in
23 Organic Thin-Film Transistors Due to Self-Assembled Monolayers at the Dielectric Surface.
24 *Adv. Funct. Mater.* **2009**, *19*, 958-967.
- 25 (30) Vasudevan, S.; Kapur, N.; He, T.; Neurock, M.; Tour, J. M.; Ghosh, A. W. Controlling
26 Transistor Threshold Voltages Using Molecular Dipoles. *J. Appl. Phys.* **2009**, *105*, 093703.
- 27 (31) Pernstich, K. P.; Haas, S.; Oberhoff, D.; Goldmann, C.; Gundlach, D. J.; Batlogg, B.;
28 Rashid, A. N.; Schitter, G. Threshold Voltage Shift in Organic Field Effect Transistors by Dipole
29 Monolayers on the Gate Insulator. *J. Appl. Phys.* **2004**, *96*, 6431-6438.
- 30 (32) Song, C. K.; Luck, K. A.; Zhou, N.; Zeng, L.; Heitzer, H. M.; Manley, E. F.; Goldman, S.;
31 Chen, L. X.; Ratner, M. A.; Bedzyk, M. J. "Supersaturated" Self-Assembled Charge-Selective
32 Interfacial Layers for Organic Solar Cells. *J. Am. Chem. Soc.* **2014**, *136*, 17762-17773.
- 33 (33) Halik, M.; Klauk, H.; Zschieschang, U.; Schmid, G.; Dehm, C.; Schütz, M.; Maisch, S.;
34 Effenberger, F.; Brunnbauer, M.; Stellacci, F. Low-Voltage Organic Transistors with an
35 Amorphous Molecular Gate Dielectric. *Nature* **2004**, *431*, 963-966.
- 36 (34) de Pauli, M.; Zschieschang, U.; Barcelos, I. D.; Klauk, H.; Malachias, A. Tailoring the
37 Dielectric Layer Structure for Enhanced Carrier Mobility in Organic Transistors: The Use of
38 Hybrid Inorganic/Organic Multilayer Dielectrics. *Adv. Electron. Mater.* **2016**, *2*, 1500402.
- 39 (35) Salinas, M.; Jager, C. M.; Amin, A. Y.; Dral, P. O.; Meyer-Friedrichsen, T.; Hirsch, A.;
40 Clark, T.; Halik, M. The Relationship between Threshold Voltage and Dipolar Character of Self-
41 Assembled Monolayers in Organic Thin-Film Transistors *J. Am. Chem. Soc.* **2012**, *134*, 12648-
42 12652.
- 43 (36) Jedaa, A.; Salinas, M.; Jäger, C. M.; Clark, T.; Ebel, A.; Hirsch, A.; Halik, M. Mixed Self-
44 Assembled Monolayer of Molecules with Dipolar and Acceptor Character—Influence on
45 Hysteresis and Threshold Voltage in Organic Thin-Film Transistors. *Appl. Phys. Lett.* **2012**, *100*,
46 36.
- 47
48
49
50
51
52
53
54
55
56
57
58
59
60

- 1
2
3 (37) Abu - Husein, T.; Schuster, S.; Egger, D. A.; Kind, M.; Santowski, T.; Wiesner, A.;
4 Chiechi, R.; Zojer, E.; Terfort, A.; Zharnikov, M. The Effects of Embedded Dipoles in Aromatic
5 Self - Assembled Monolayers. *Adv. Funct. Mater.* **2015**, *25*, 3943-3957.
- 6 (38) Wang, B.; Di Carlo, G.; Turrisi, R.; Zeng, L.; Stallings, K.; Huang, W.; Bedzyk, M. J.;
7 Beverina, L.; Marks, T. J.; Facchetti, A. The Dipole Moment Inversion Effects in Self-
8 Assembled Nanodielectrics for Organic Transistors. *Chem. Mater.* **2017**, *29*, 9974-9980.
- 9 (39) Nelson, A. Co-Refinement of Multiple-Contrast Neutron/X-Ray Reflectivity Data
10 Usingmotofit. *J. Appl. Crystallogr.* **2006**, *39*, 273-276.
- 11 (40) Bedzyk, M. J.; Bilderback, D. H.; Bommarito, G. M.; Caffrey, M.; Schildkraut, J. S. X-Ray
12 Standing Waves - a Molecular Yardstick for Biological-Membranes. *Science* **1988**, *241*, 1788-
13 1791.
- 14 (41) Bedzyk, M. J.; Libera, J. A.: X-Ray Standing Wave in Multilayers. In *Synchrotron*
15 *Radiation Techniques and Applications: The X-Ray Standing Wave Technique: Principles and*
16 *Applications*; Zegenhagen, J., Kazimirov, A., Eds.; World Scientific, 2013; Vol. 7.
- 17 (42) Ghose, S. K.; Dev, B. N. X-Ray Standing Wave and Reflectometric Characterization of
18 Multilayer Structures. *Phys. Rev. B* **2001**, *63*.
- 19 (43) Wu, L.; Liu, Y.; Wang, X.; Wang, G.; Zhao, D.; Chen, G. X-Ray Standing Wave Enhanced
20 Scattering from Mesoporous Silica Thin Films. *Appl. Phys. Lett.* **2017**, *110*, 041603.
- 21 (44) Ohtomo, M.; Yamauchi, Y.; Sun, X.; Kuzubov, A. A.; Mikhaleva, N. S.; Avramov, P. V.;
22 Entani, S.; Matsumoto, Y.; Naramoto, H.; Sakai, S. Direct Observation of Site-Selective
23 Hydrogenation and Spin-Polarization in Hydrogenated Hexagonal Boron Nitride on Ni (111).
24 *Nanoscale* **2017**, *9*, 2369-2375.
- 25 (45) Lin, W.; Lee, T. L.; Lyman, P. F.; Lee, J.; Bedzyk, M. J.; Marks, T. J. Atomic Resolution X-
26 Ray Standing Wave Microstructural Characterization of Nlo-Active Self-Assembled
27 Chromophoric Superlattices. *J. Am. Chem. Soc.* **1997**, *119*, 2205-2211.
- 28 (46) Libera, J. A.; Gurney, R. W.; Schwartz, C.; Jin, H.; Lee, T. L.; Nguyen, S. T.; Hupp, J. T.;
29 Bedzyk, M. J. Comparative X-Ray Standing Wave Analysis of Metal-Phosphonate Multilayer
30 Films of Dodecane and Porphyrin Molecular Square. *J. Phys. Chem. B* **2005**, *109*, 1441-1450.
- 31 (47) Libera, J. A.; Cheng, H.; de la Cruz, M. O.; Bedzyk, M. J. Direct Observation of Cations
32 and Polynucleotides Explains Polyion Adsorption to Like-Charged Surfaces. *J. Phys. Chem. B*
33 **2005**, *109*, 23001-23007.
- 34 (48) Parratt, L. G. Surface Studies of Solids by Total Reflection of X-Rays. *Phys. Rev.* **1954**, *95*,
35 359-369.
- 36 (49) Bedzyk, M. J. New Trends in X-Ray Standing Waves. *Nucl. Instr. Meth. Phys. Res.* **1988**,
37 *A266*, 679-683.
- 38 (50) Bedzyk, M. J.; Bilderback, D.; White, J.; Abruna, H. D.; Bommarito, M. G. Probing
39 Electrochemical Interfaces with X-Ray Standing Waves. *J. Phys. Chem.* **1986**, *90*, 4926-4928.
- 40 (51) Born, M.; Wolf, E. Principles of Optics, Seventh Expanded Edition. *Cambridge, England*
41 **1999**.
- 42 (52) Kresse, G.; Furthmüller, J. Efficient Iterative Schemes for Ab Initio Total-Energy
43 Calculations Using a Plane-Wave Basis Set. *Phys.Rev. B* **1996**, *54*, 11169.
- 44 (53) Kresse, G.; Furthmüller, J. Efficiency of Ab-Initio Total Energy Calculations for Metals and
45 Semiconductors Using a Plane-Wave Basis Set. *Comput. Mater. Sci.* **1996**, *6*, 15-50.
- 46
47
48
49
50
51
52
53
54
55
56
57
58
59
60

TOC Graphic

